

pubs.acs.org/NanoLett Letter

# Exciton Dipole Orientation of Strain-Induced Quantum Emitters in WSe<sub>2</sub>

Yue Luo,\* Na Liu, Bumho Kim, James Hone, and Stefan Strauf\*



Cite This: Nano Lett. 2020, 20, 5119-5126



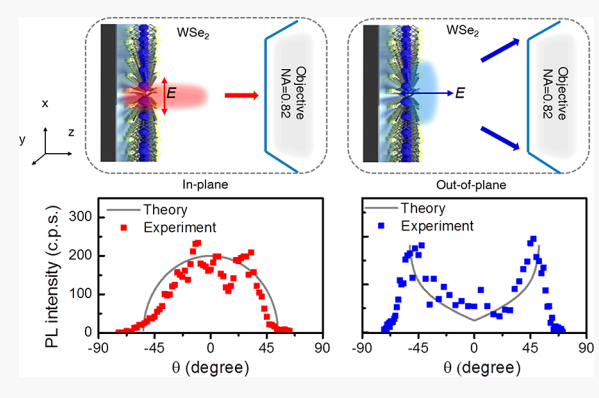
**ACCESS** 

Metrics & More

Article Recommendations

Supporting Information

**ABSTRACT:** Transition metal dichalcogenides are promising semi-conductors to enable advances in photonics and electronics and have also been considered as a host for quantum emitters. Particularly, recent advances demonstrate site-controlled quantum emitters in WSe<sub>2</sub> through strain deformation. Albeit essential for device integration, the dipole orientation of these strain-induced quantum emitters remains unknown. Here we employ angular-resolved spectroscopy to experimentally determine the dipole orientation of strain-induced quantum emitters. It is found that with increasing local strain the quantum emitters in WSe<sub>2</sub> undergo a transition from in-plane to out-of-plane dipole orientation if their emission wavelength is longer than 750 nm. In addition, the exciton g-factor remains with average values of  $g = 8.52 \pm 1.2$  unchanged in the entire emission wavelength. These findings provide experimental support



of the interlayer defect exciton model and highlight the importance of an underlying three-dimensional strain profile of deformed monolayer semiconductors, which is essential to optimize emitter-mode coupling in nanoplasmonics.

KEYWORDS: 2D materials, quantum emitter, angular-resolved spectroscopy, exciton dipole orientation, cavity coupling, g-factor

# **■ INTRODUCTION**

Transition metal dichalcogenides (TMDs) are promising semiconductors to enable advances in photonics and electronics. 1,2 In their two-dimensional (2D) monolayer form, TMDs exhibit a direct bandgap and large exciton binding energies leading to bright optical emission.<sup>3</sup> Particularly, tungsten diselenide (WSe<sub>2</sub>) has gained considerable interest as a host of single-photon emitters (SPEs) to realize on-chip photonic quantum technologies. 4-6 Initially, SPEs in WSe2 were discovered being randomly distributed in optical hot-spots of unknown microscopic origin.<sup>7-11</sup> Later work showed the connection between local strain and resulting redshift of the zero-dimensional (0D) exciton formation, which has led to a unique strain engineering of SPE in monolayer WSe<sub>2</sub> via point-like stressors such as nanobubbles<sup>13</sup> and lithographically defined nanopillars, 14,15 or line-like stressors such as elongated wrinkles that under controlled piezoelectric actuation show SPE emission energy shifts up to 18 meV. 16 The advent of site-controlled quantum emitters in WSe<sub>2</sub> has also led to the recent demonstration of a  $3 \times 4$  array of SPE that is deterministically coupled to vertical gap-mode plasmonic nanocavities, displaying more than 500-fold Purcell enhancement of the spontaneous emission.<sup>17</sup> A direct consequence of a large Purcell enhancement is that nonradiative emission channels can be effectively overcome, giving rise to drastically improved SPE quantum yields (QYs) from 1 to 2% to a cavity-enhanced QY up to 65%, 17 which also

enables generation of single-photon emission up to temperatures of 160 K for the case of WSe<sub>2</sub>. <sup>18</sup>

Despite these promising optical properties of strain-induced SPE and their prospects for device integration, the underlying microscopic mechanisms involved in the 0D exciton emission are still investigated. In contrast, the optical properties of the 2D excitons recombining out of the  $K^{\pm}$  valleys are well understood, with exciton-photon coupling following the chiral optical selection rules (spin-valley locking) in theory 19 while in experimental systems softening of the selection rule can be caused by disorder, local strain, or material tilting. Specifically, in WSe<sub>2</sub>, the electron spin orientations in the lower conduction band (CB) and in the upper valence band (VB) are opposite. As a result, the upper CB to upper VB transition is spinallowed, giving rise to the bright 2D exciton emission (X<sup>0</sup>) with a corresponding in-plane dipole moment. Likewise, the lower CB to upper VB transition is spin-forbidden, giving rise to the dark 2D exciton emission (X<sup>Dark</sup>) with a corresponding out-of-plane dipole moment, making excitation and detection with a typical light path perpendicular to the monolayer plane

 Received:
 March 30, 2020

 Revised:
 June 17, 2020

 Published:
 June 18, 2020





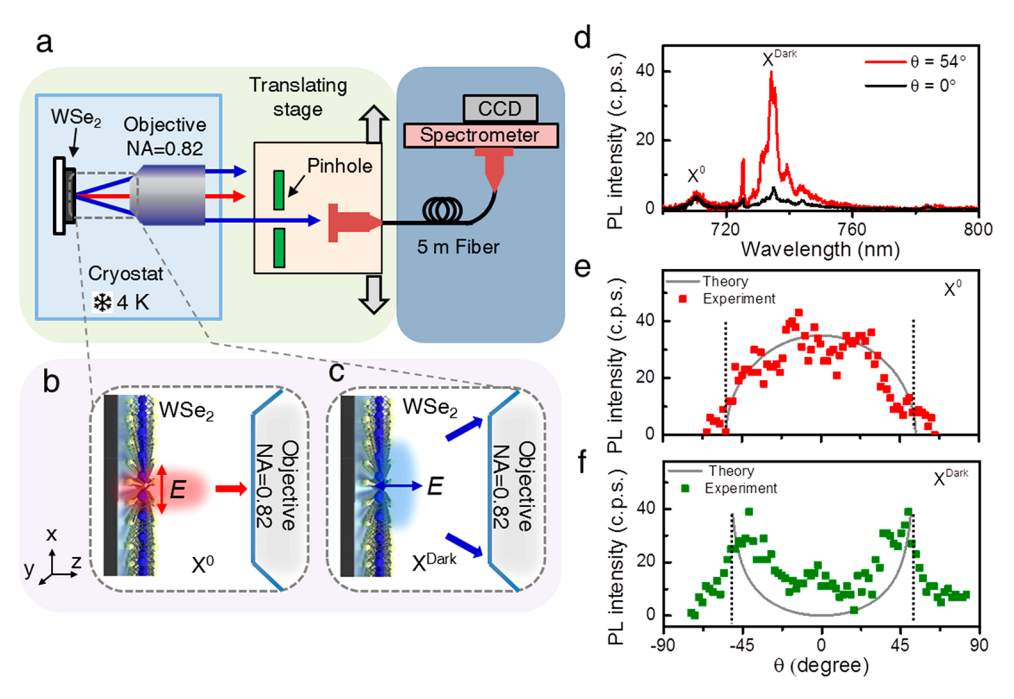


Figure 1. Overview of angular-resolved detection on 2D bright and dark excitons. (a) Schematic of the optical setup that enables filtering of detection angles  $\theta$ . A 100  $\mu$ m pinhole on a translating stage is used to allow only a certain detection angle  $\theta$ . (b) Sketch of a 2D bright exciton in monolayer WSe<sub>2</sub> with in-plane orientation (red double-arrow) and light propagation along the z-direction. (c) Sketch of a 2D dark exciton in monolayer WSe<sub>2</sub> with out-of-plane orientation (blue double-arrow) and in-plane light propagation. (d) PL spectra of 2D neutral exciton ( $X^0$ ) and dark exciton ( $X^{Dark}$ ) taken at 0° (black solid line) and 54° (red solid line) detection angle. The intensity of  $X^0$  is magnified 3-fold for illustration. (e) Intensities of  $X^0$  as a function of the filtered angle. (f) Intensities of  $X^{Dark}$  as a function of the filtered angle. Gray solid lines are a theoretical model of the intensity functions for in-plane and out-of-plane dipole emitter orientation, respectively. The dashed lines in parts e and f indicate an objective aperture of  $\pm 54^\circ$ .

challenging. Nevertheless, the use of near-field coupling to surface plasmon polaritons or the utilization of microscope objectives with high numerical aperture (NA) as well as direct in-plane optical excitation and detection geometries revealed strong optical emission from  $X^{Dark}$  states in the corresponding optical spectra. <sup>21</sup>

The question arises of whether or not the strain-induced 0D SPE will simply inherit the spin-valley physics and exciton dipole orientation of the 2D bright and dark exciton species or if a more complex microscopic mechanism involving defect states is responsible for the strain-induced SPE formation. Two experimental observations pinpoint that the latter scenario is more likely. First, if the substrate-induced strain potential is absent, i.e., the monolayer appears flat and unstrained in atomic-force microscope imaging, there remains a weak and spectrally broad optical emission centered around 742 nm, i.e., energetically below the X<sup>0</sup> and X<sup>Dark</sup> states, which is likely associated with emission from excitons localized at point defects. 13 Second, the advent of flux-grown WSe<sub>2</sub> material with significantly reduced intrinsic point defect densities<sup>22</sup> reveals a drastically improved QY for the 0D exciton emission, with values up to QY = 32% of the pristine material (without plasmonic enhancement), compared to chemical vapor deposition grown WSe<sub>2</sub> limited to QYs of 1-2%.<sup>17</sup> Both findings suggest that point defects play an important role in the SPE formation. The recent theory model by Linhart et al. proposes a unifying mechanism in the form of intervalley defect exciton (IDE) emission.<sup>23</sup> In this model, the local strain from nanobubbles or pillars energetically pulls down the darkstate conduction band associated with the X<sup>Dark</sup> transition, which hybridizes with the defect state associated with

omnipresent intrinsic Se vacancies. This hybridization breaks the spin-valley locking, thereby leading to efficient radiative decay of the IDE that appears in optical spectra with a characteristic doublet with a predicted zero-field splitting  $\Delta_0$  of about 0.8–2 meV and an exciton g-factor of g=8.8, that is considered the source of the observed 0D SPE in WSe<sub>2</sub>.

One of the limitations of the model by Linhart et al. <sup>23</sup> is that the strain profile is assumed to be restricted to the *xy*-plane of the monolayer material, while nanobubbles and nanopillars stick typically out of the plane by about 20–200 nm, creating a 3D strain profile in WSe<sub>2</sub>. The dipole emitter orientation of 0D SPE has not yet been investigated experimentally, albeit being essential from a fundamental point of view to uncover the microscopic origin of SPE in 3D topographies as well as from a practical point of view when coupling quantum emitters to nanocavity modes.

Here we employ angular-resolved imaging to determine the dipole orientation of 0D SPEs in WSe<sub>2</sub> that are strain-induced via formation of nanobubbles. We show a transition from inplane to out-of-plane dipole moment orientation for the defect excitons if their emission wavelength is longer than around 750 nm, while the exciton g-factor remains with average values of g =  $8.52 \pm 1.2$  largely unchanged in the entire emission wavelength regime from 720 to 800 nm. We further discuss these findings in the framework of the IDE emission and provide guidance toward optimizing cavity—emitter coupling of strain-induced SPE with respect to nanoplasmonic gapmode cavities.

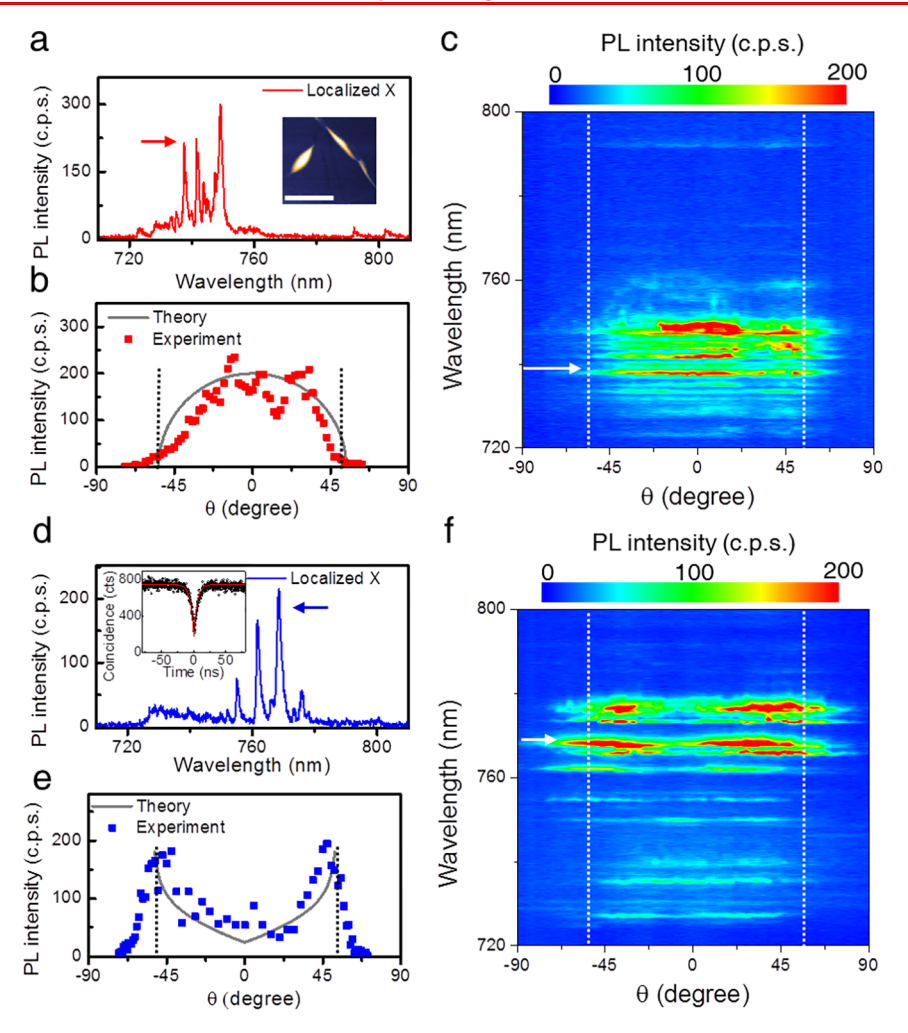


Figure 2. Determination of dipole orientation for 0D strain-induced excitons. (a) PL spectra of localized excitons with a wavelength shorter than 750 nm. Inset: atomic force microscope image featuring nanofolds. Scale bar: 500 nm. (b) Angular dependence of the PL intensity for a quantum emitter with an emission wavelength of 747 nm (red arrow in part a). The gray line is the theoretical fit. (c) Mapping of PL intensities versus collection angles at exemplary location 1. (d) PL spectra of localized excitons with a wavelength longer than 750 nm. Inset: Open black dots are second-order photon correlation traces  $g^{(2)}(\tau)$  recorded with a Hanbury Brown–Twiss setup under nonresonant excitation. The red solid line is a fit to the standard rate equation of a two-level system. (e) Angular dependence of PL intensity for a quantum emitter with an emission wavelength of 768 nm (blue arrow in part d). Gray solid lines are a theoretical model of the intensity functions for in-plane and out-of-plane dipole emitter orientation, respectively. (f) Mapping of PL intensities under different collection angles at exemplary location 2. The dashed lines indicate a microscope objective aperture of  $\pm 54^{\circ}$ .

# RESULTS

Lieb et al. introduced a technique to detect the threedimensional dipole orientation of single-molecule quantum emitters held at room temperature based on direct imaging of the intensity emission pattern in the back-focal plane of a high NA objective lens. <sup>24</sup> In our system, the objective (NA = 0.82)is placed inside a closed cycle cryogenic system (attodry1100) to allow dipole-orientation measurements for quantum emitters held at 4 K. Since the cryogenic setup requires light collection with an optical fiber to reach the spectrometer and CCD detector, we follow here a modified technique utilized by Wang et al.<sup>21</sup> based on pinhole scanning in the parallel beam path. As shown schematically in Figure 1, the 100  $\mu$ m pinhole is placed in the parallel beam path and scanned with a motorized translating stage to record PL spectra that are spatially selected with respect to the light emission angle from the surface, with an angular resolution of 3.8°. Note that since the pinhole is only placed at the detection path, which is separated from the excitation path by a beam splitter (not

shown), there is no variation of excitation intensity while moving the translating stage with the pinhole. When the filtering pinhole is located at the center ( $\theta = 0^{\circ}$ ), photons emitted in the *z*-direction can pass through the pinhole and reach the detector. In contrast, when the pinhole is moved toward the edge of the objective aperture ( $\theta = 54^{\circ}$ ), photons that are emitted into the far-field by the dipole with x-y plane orientation can be collected more effectively through the pinhole.

As a calibration test to confirm that our optical setup can resolve the orientation of exciton dipole emitters in WSe<sub>2</sub>, we first measured the spatially uniformly distributed 2D exciton emissions, X<sup>0</sup> and X<sup>Dark</sup>, that are well-known to have in-plane (Figure 1b) and out-of-plane (Figure 1c) dipole moments, respectively.<sup>21</sup> Figure 1d presents the PL spectra that are normalized to the intensity of the X<sup>0</sup> peak (713 nm) recorded under two extreme configurations, when the pinhole is placed at  $\theta = 0^{\circ}$  position and  $\theta = 54^{\circ}$  position, respectively. As expected, the X<sup>Dark</sup> (734 nm) emission peak vanishes at 0°

detection setting but appears to be maximized at  $\theta=54^\circ$  detection, indicating an out-of-plane dipole moment for  $X^{Dark}$ . In addition, we carried out a line scan by moving the pinhole from  $\theta=-54^\circ$  to  $\theta=54^\circ$  to reveal the propagation directions between light from  $X^0$  and  $X^{Dark}$ , as shown in Figure 1e and f. We also fit the pattern using the model proposed by Lieb et al.  $^{24}$  for dipole emitters with in-plane and out-of-plane orientation, as shown by the gray solid lines. It is clear that  $X^0$  is maximized for  $\theta=0^\circ$  (in-plane dipole orientation), whereas the  $X^{Dark}$  transition is only visible for large  $\theta$  (out-of-plane dipole orientation). Note that the sharp intensity decay beyond  $\pm 54^\circ$  (outside of the vertical dashed lines) is an artifact caused by the finite aperture of the objective; i.e., light leaving the sample surface with larger emission angles does not transmit through the system.

We now apply this technique to study the dipole orientation of localized excitons (0D excitons), particularly with respect to strain-induced 0D exciton quantum emitters in WSe<sub>2</sub>. 12,14,15 One simple way to create 0D excitons in monolayer WSe2 is based on the deliberate formation of nanobubbles and folds via cold-stamping and hard pressing, as we recently demonstrated. 13 As shown in the inset of Figure 2a, atomic force microscope (AFM) images show the formation of several nanobubbles and folds occurs within the excitation laser spot area with heights varying from 20 to 80 nm as well as lateral diameter of nanobubbles typically varying from 200 to 500 nm. 13 The associated 3D strain profile is significantly more extended than the exciton Bohr radius in WSe2. The corresponding PL spectrum from the first location in Figure 2a shows sharp peaks from 0D excitons with transition wavelengths shorter than 750 nm, i.e., predominantly from weakly localized 0D exciton emission near the ensemble distribution of the defect emission. To verify the quantum light signature, we recorded the second-order photon correlation function  $g^{(2)}(\tau)$  of the spectrally filtered single sharp peak, with one example of pronounced single-photon antibunching shown in the inset of Figure 2d. The zero-delay time value of  $g^2(0) =$  $0.24 \pm 0.01$  is comparable to our previous findings for nanobubble- or nanopillar-induced 0D excitons. 13,17,18 reveal the dipole orientation of the 0D localized excitons, we carried out the angular-resolved scanning of the PL emission profile for the quantum emitter emitting at 747 nm (Figure 2b). Clearly, the PL intensity of this quantum emitter is maximized at  $\theta = 0^{\circ}$  following a similar pattern as was observed for the X<sup>0</sup> transition (Figure 1), indicating an underlying in-plane dipole moment in this case. The angularresolved PL intensity map in Figure 2c reveals that a number of other quantum emitters in the same wavelength regime follow a similar pattern indicative for in-plane dipole orientation.

In strong contrast, laser excitation at other locations on the same sample reveals optical emission spectra with predominantly 0D quantum emitters that emit at wavelengths longer than 750 nm (Figure 2d), which have been suggested to originate from strain-induced excitons formed by energetically deeper potentials. In this case, pinhole scanning reveals a clear pattern of dark-state exciton emission, where the maxima of PL intensity for the 768 nm emission are at the edges of the objective aperture near  $\theta=\pm54^{\circ}$  (Figure 2e), similar to the  $X^{\text{Dark}}$  state emission for the case of 2D excitons (Figure 1). This contrasting behavior is also valid for the other quantum emitters that emit at wavelengths longer than 750 nm, as shown in Figure 2f, and demonstrates that deeply localized 0D excitons feature an out-of-plane dipole moment orientation. In

addition, both in-plane and out-of-plane cases can also be observed at the same excitation location within the 1  $\mu$ m laser spot size. To illustrate this, Figure 3a shows a magnified view

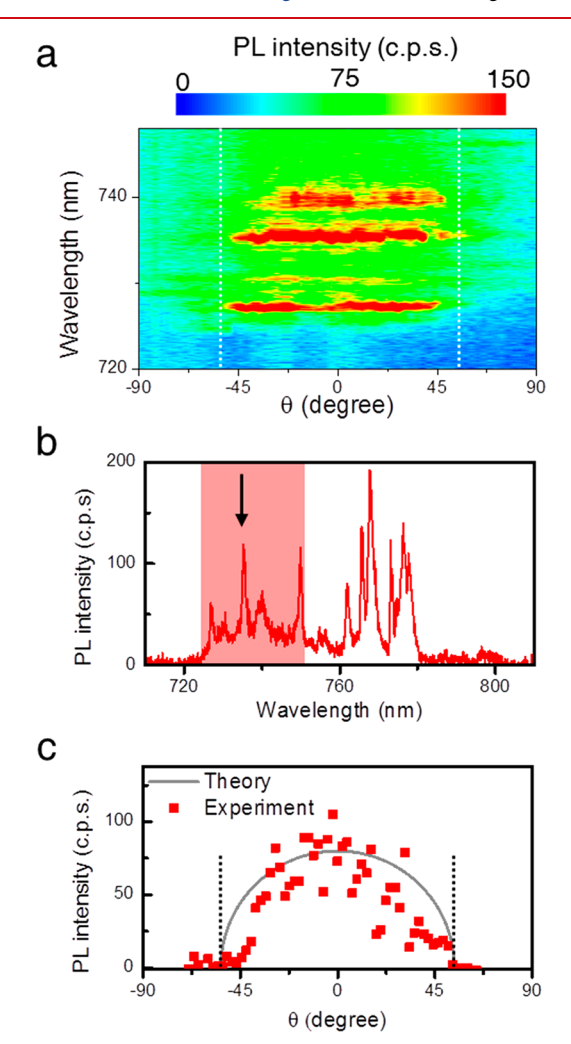


**Figure 3.** Different dipole polarization at the same excitation position. (a) Zoom-in and rescaled PL mapping from Figure 2f for the emission wavelength from 720 to 750 nm at spot 2. (b) PL spectra of localized exciton emission within a range of 720–800 nm with a detection angle of 22.5° to show both in-plane and out-of-plane emissions. (c) Angular dependence of the PL intensity of an emitter with an emission wavelength of 736 nm (black arrow in part b). The gray solid line is a theoretical model of the intensity functions for in-plane dipole emitter orientation. Dashed lines indicate the microscope objective aperture of  $\pm 54^\circ$ .

of the data from Figure 2f centered to the emission occurring at shorter wavelength. For the quantum emitter highlighted in Figure 3b (solid arrow at 736 nm), the pinhole scan reveals that the PL intensity is maximized at near  $\theta=0^\circ$  detection angle (Figure 3), implying in-plane and out-of-plane dipole orientations can coexist within the excitation area.

To demonstrate that the transition from in-plane to out-of-plane is strongly correlated to the emission wavelength, we have analyzed 20 strain-induced quantum emitters in the wavelength range from 730 to 780 nm. One way to quantify the dipole orientation from the angular-resolved scans is to define the intensity visibility as  $V = (I_{0^{\circ}} - I_{54^{\circ}})/(I_{0^{\circ}} + I_{54^{\circ}})$ , where  $I_{0^{\circ}}$  and  $I_{54^{\circ}}$  are the PL intensity at a detection angle of  $\theta = 0^{\circ}$  and  $\theta = 54^{\circ}$ , respectively. For the exciton transitions with

predominant in-plane dipole orientation, one expects to find  $I_0 > I_{54^{\circ}}$  and thus a positive visibility V. Likewise, for predominant out-of-plane orientation, V will be negative. Figure 4a shows

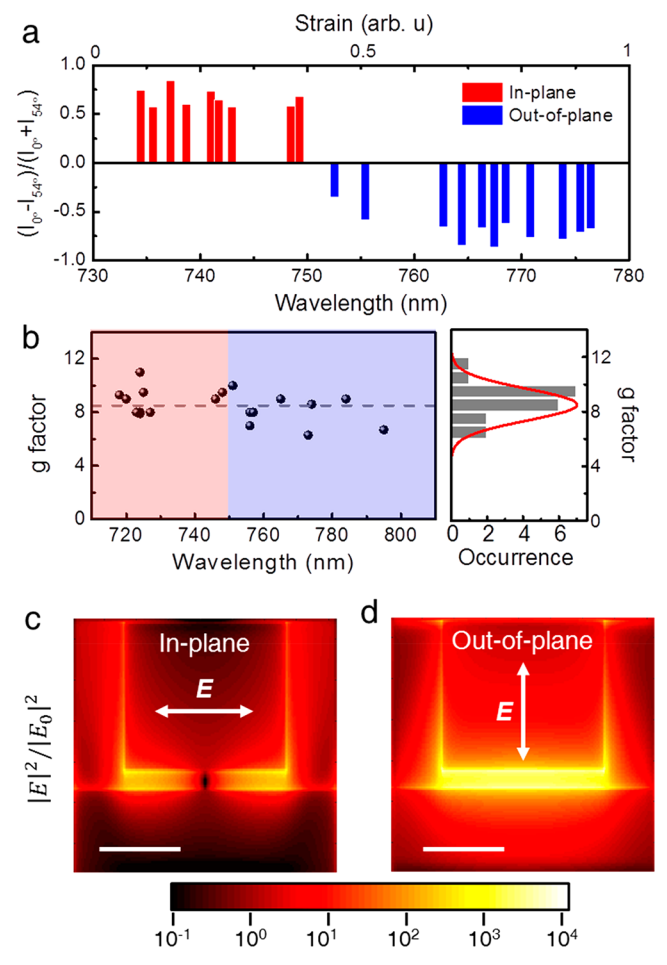


Figure 4. Statistics of dipole-orientation visibility V and g-factor for strain-induced quantum emitters. (a) Bar-plot of intensity visibility V for 20 quantum emitters calculated from the intensity extinction ratio  $(I_{0^{\circ}}-I_{54^{\circ}})/(I_{0^{\circ}}+I_{54^{\circ}})$  determined from angular-resolved imaging. Inplane oriented excitons are colored in red, while out-of-plane oriented excitons are colored in blue. (b) Statistics of g-factors for 18 strain-induced quantum emitters (left panel). The gray dashed line shows the average g-factor of  $8.52 \pm 1.2$ . The right panel shows the corresponding histogram of the g-factor, and the red solid line is the normal distribution fit. (c, d) Side-view of simulated electric-field intensity enhancement  $(|E|^2/|E_0|^2)$  profile of in-plane (c) and out-of-plane (d) light with the finite-difference time-domain method. Scale bar: 50 nm.

the corresponding visibility values where bars are colored in red for V > 0 and blue for V < 0. For the localized excitons that emit at shorter wavelength, V varies from 0.57 to 0.85, showing clearly in-plane dipole orientation in all cases. Below 750 nm, a transition occurs, with V becoming negative and varying from -0.86 to -0.38, implying out-of-plane dipole orientation in all cases. In the transition regime around 753 nm, the visibility drops to the lowest values, indicating that those quantum emitters are in a mixed state with respect to their dipole orientation.

To investigate the hypothesis that the observed dark-state behavior of the localized excitons emitting at a wavelength longer than 750 nm originates from point defects that have a largely different electronic structure, we have determined the exciton g-factor via magneto-PL measurements. To this end, the magnetic field B was applied parallel to the k-vector of the incident laser (Faraday configuration). All spectra of straininduced quantum emitters display a zero-field splitting  $\Delta_0$  that varies between 400 and 800  $\mu eV$ , with an average value of 677 ueV, that further splits apart in an applied magnetic field following the well-known Zeeman effect relation:  $\Delta_{\rm B} = \sqrt{(\Delta_0)^2 + (\mu_{\rm B} g B)^2}$ , where  $\mu_{\rm B}$  is the Bohr magneton and g is the exciton g-factor. The g-factors for 18 quantum emitters determined in this way are displayed in Figure 4b, revealing an average g-factor of  $8.52 \pm 1.2$ , which is in good agreement with experimental values reported for localized excitons in monolayer  $WSe_2$ . Importantly, the narrow distribution centered around  $g = 8.52 \pm 1.2$  indicates that the underlying electronic structure does not change considerably over the entire wavelength range, which is in excellent agreement with the theory model by Linhart et al., 23 which estimated values of g = 8.8 for the localized intervalley defect excitons. We also note that other possible reservoirs for the quantum emitter hybridization exist, including momentumdark excitons in the QK valley<sup>25</sup> or KK' valley<sup>26</sup> with g-factors of 7 and 11 for spin-like and spin-unlike QK excitons and 12 for KK' excitons<sup>27</sup> or 9 for spin-unlike KK excitons.<sup>28</sup> Given the narrow distribution of  $g = 8.52 \pm 1.2$  in our work, those momentum-dark 2D excitons with g = 11-12 are less likely to contribute to the defect state emission. Likewise, we can rule out that the strain-induced quantum emitter in the wavelength range from 720 to 750 nm inherits the observed bright-state behavior from the corresponding 2D X<sup>0</sup> exciton, since this electronic state is characterized by a factor of 2 smaller exciton g-factor of typically g = 4-5. However, based on the gfactor argument, we cannot fully rule out that momentum-dark excitons can contribute in addition to the spin-dark excitons as a mechanism to brighten the localized defect exciton emission.

Regardless of the microscopic origin, which is still not fully uncovered in the theoretical literature, we would like to point out that the experimental observed transition of the dipole moment from in-plane to out-of-plane with increasing wavelength in Figure 4a is quite systematic and coincides with a pronounced structural change, i.e., the tilting of the monolayer material itself into an out-of-plane configuration at regions of highest strain. That the maximum strain is located near the edge of the stressor is apparent from our recent work showing that experimentally with highest likelihood exactly four 0D SPE will be induced with a cubic stressor, in agreement with strain hot-spots in numerical simulations located around the four corners of a cube. Furthermore, the monolayers are tilted out-of-plane at the stressor edge before bending back down flat onto the substrate, as is evident in scanning electron microscope images.<sup>17</sup> In addition, recent scanning near-field spectroscopy with sub-20 nm spatial resolution reveals also for nanobubbles that the regions of highest strain are located at the tilted edge periphery of nanobubble stressors and not at the flat center.<sup>31</sup> We therefore interpret the observed transition from in-plane to out-of-plane dipole orientation for wavelengths longer than 750 nm to reflect the local curvature change in the presence of nanocubes or point-like nanobubbles, which effectively rotates the WSe<sub>2</sub> monolayer itself out of plane along the periphery that hosts the highest strain (largest redshift).

Applications in quantum information science favor typically those quantum emitters emitting at longer wavelength, since they are separated far enough from the ensemble emission, resulting under moderate spectral filtering in higher singlephoton purity, where  $g^{(2)}(\tau = 0)$  approaches zero. Knowledge of the dipole orientation of the quantum emitters is further crucial when engineering the spontaneous emission rate (Purcell effect) and quantum yield via coupling to optical cavity modes. Of particularly recent interest are plasmonic gapmode-type nanocavities<sup>32</sup> that achieve ultrahigh Purcell enhancement up to 1000-fold<sup>33,34</sup> as well as deterministic spatial coupling with quantum emitters.<sup>17</sup> Interestingly, the nanoparticle-on-metal geometry supports both in-plane and out-of-plane dipole orientations, albeit with unequal coupling strength. To illustrate this, we used finite-difference timedomain simulations to calculate the field intensity profile when driven under in-plane and out-of-plane polarization orientation. Figure 4c shows the side-view of the profile for the inplane field enhanced by the plasmonic gap-mode, resulting in an electric-field-intensity enhancement EF =  $|E|^2/|E_0|^2$  = 910. In contrast, for the case of an out-of-plane dipole moment coupled to the plasmonic gap-mode, the enhancement factor can be nearly 2 orders of magnitude higher, with EF = 4640 (Figure 4d). The coupling strength is apparently significantly larger when the field direction of the quantum emitter is perpendicular to the metal surface plane, as is the case for strain-induced quantum emitters in WSe2 emitting at wavelengths longer than 750 nm. Our findings in Figure 4a of an out-of-plane dipole configuration for strongly localized 0D quantum emitters provide a solid foundation for our recent report of strong Purcell enhancement for spatially deterministic coupled quantum emitters to vertical plasmonic gap-mode nanocavities.<sup>17</sup> On the other hand, if it is required to Purcellenhance in-plane dipoles such as the quantum emitters at shorter wavelength (720-750 nm), the better approach is to use the horizontal plasmonic gap-mode provided by bowtietype plasmonic nanocavity modes, 35,36 since the nanoparticleon-metal-type system provides only limited Purcell enhancement for this case.

In conclusion, we have shown that strain-induced quantum emitters in WSe2 undergo a transition from in-plane to out-ofplane dipole moment orientation if their emission wavelength is longer than 750 nm. In contrast, the exciton g-factor remains with average values of  $g = 8.52 \pm 1.2$  largely unchanged in the entire emission wavelength regime from 720 to 800 nm. These findings suggest that the dipole moment orientation of straininduced excitons follows the local curvature change in the presence of nanobubbles, folds, or nanopillars, which effectively rotates the WSe2 monolayer itself out of plane in the presence of highest strain. Our findings provide important insights into the interplay of topography, strain, and energy level hybridization for 0D quantum emitters in WSe2, which is not only relevant to optimize emitter-mode coupling for plasmonic nanocavities, 17 but also for other interactions such as magnetic proximity coupling<sup>37</sup> or coupling between distinct emitters mediated by short-range Coulomb interaction.<sup>38</sup> While recent advances in nanoscale strain engineering of monolayer semiconductors already provide spatial scalability of cavity-coupled SPE required to enable complex on-chip quantum information processing architectures, further progress is likely to realize room temperature operation as well as singlephoton indistinguishability toward enabling quantum logic.3

#### METHODS

**Exfoliation and Transfer.** Monolayers of WSe $_2$  were mechanically exfoliated from crystals grown by the chemical vapor transport (CVT) technique (HQ graphene). Before transfer, the exfoliated layers are attached to a viscoelastic stamp (gel-film). The exfoliated layers are then dry-transferred onto the silicon substrate with 285 nm of SiO $_2$  on top. We use an optical microscope to distinguish the monolayers and multilayers by the optical contrast.

**Photoluminescence Spectroscopy.** Micro-photoluminescence ( $\mu$ -PL) measurements were performed using a closed-cycle cryogen-free cryostat (attodry1100, attocube systems AG) where the sample temperature was set to 3.8 K. The excitation source was a laser diode operating at 532 nm in continuous wave mode. We collect the exciton emission with an infinity-corrected apochromatic microscope objective lens and collimate the light into a parallel beam. The output is sent into a 5 m long optical fiber which is attached to a spectrometer (0.75 m focal length, 300 groove/mm grating, and 150  $\mu$ m slit width) with a liquid-nitrogen-cooled CCD camera (Princeton Instruments). Magnetic fields were applied perpendicular to the plane of the sample within the range 0–9 T to determine the *g*-factor and fine structure splitting from the Zeeman pattern.

**Angular-Resolved Spectroscopy.** In addition to the  $\mu$ -PL setup, we follow the raster-scan method in ref 21 to gain information on the angular distribution of the quantum emitter emission. Unlike the conventional back-focal plane microscopy<sup>24</sup> that directly images the back-focal plane, we use a 100 µm pinhole mounted on a motorized translating stage with a step size of 50  $\mu$ m (accuracy 1  $\mu$ m) over a range of 3.6 mm to cover the entire parallel beam spot of 3 mm diameter from the cryogenic objective inside the attodry1100, while the scanning setup is attached on a local breadboard on top of the cryostat. Note we use only the cryogenic microscope objective followed by the pinhole at a distance of about 1.5 m from the objective and not another lens to image onto the pinhole like in ref 21. A fiber coupler is mounted after the pinhole fixed to the optical axis to collect the transmitted light signal into a 5 m multimode optical fiber. The output from the fiber is sent into the spectrometer/CCD system.

# ASSOCIATED CONTENT

# Supporting Information

The Supporting Information is available free of charge at https://pubs.acs.org/doi/10.1021/acs.nanolett.0c01358.

Discussion of emission angle calibration and additional measurement on laser reflection pattern and discussion of fine structure splitting with statistical analysis (PDF)

#### AUTHOR INFORMATION

# **Corresponding Authors**

Yue Luo — Department of Physics and Center for Quantum Science and Engineering, Stevens Institute of Technology, Hoboken, New Jersey 07030, United States; Center for Nanoscale Systems and Department of Physics, Harvard University, Cambridge, Massachusetts 02138, United States; orcid.org/0000-0002-2757-5395; Email: yue\_luo@fas.harvard.edu

**Stefan Strauf** – Department of Physics and Center for Quantum Science and Engineering, Stevens Institute of Technology,

Hoboken, New Jersey 07030, United States; orcid.org/0000-0002-9887-7059; Email: strauf@stevens.edu

#### **Authors**

Na Liu – Department of Physics and Center for Quantum Science and Engineering, Stevens Institute of Technology, Hoboken, New Jersey 07030, United States

Bumho Kim – Department of Mechanical Engineering, Columbia University, New York, New York 10027, United States

James Hone – Department of Mechanical Engineering, Columbia University, New York, New York 10027, United States

Complete contact information is available at: https://pubs.acs.org/10.1021/acs.nanolett.0c01358

#### **Notes**

The authors declare no competing financial interest.

### ACKNOWLEDGMENTS

Primary support for this work was provided by the National Science Foundation (NSF) under award DMR-1809235 (Stevens Institute of Technology) and DMR-1809361 (Columbia University). Synthesis of WSe<sub>2</sub> crystals was supported by the NSF MRSEC program through Columbia in the Center for Precision Assembly of Superstratic and Superatomic Solids (DMR-1420634). S.S. acknowledges financial support for the attodry1100 under NSF award ECCS-MRI-1531237.

# REFERENCES

- (1) Manzeli, S.; Ovchinnikov, D.; Pasquier, D.; Yazyev, O. V.; Kis, A. 2D transition metal dichalcogenides. *Nat. Rev. Mater.* **2017**, *2*, 17033.
- (2) Mak, K. F.; Shan, J. Photonics and optoelectronics of 2D semiconductor transition metal dichalcogenides. *Nat. Photonics* **2016**, 10, 216–226.
- (3) Mak, K. F.; Lee, C.; Hone, J.; Shan, J.; Heinz, T. F. Atomically Thin MoS<sub>2</sub>: A New Direct-Gap Semiconductor. *Phys. Rev. Lett.* **2010**, 105, 136805.
- (4) Aharonovich, I.; Englund, D.; Toth, M. Solid-state single-photon emitters. *Nat. Photonics* **2016**, *10*, 631–641.
- (5) Toth, M.; Aharonovich, I. Single Photon Sources in Atomically Thin Materials. *Annu. Rev. Phys. Chem.* **2019**, *70*, 123–142.
- (6) Chakraborty, C.; Vamivakas, N.; Englund, D. Advances in quantum light emission from 2D materials. *Nanophotonics* **2019**, 8, 2017.
- (7) He, Y.-M.; Clark, G.; Schaibley, J. R.; He, Y.; Chen, M.-C.; Wei, Y.-J.; Ding, X.; Zhang, Q.; Yao, W.; Xu, X.; Lu, C.-Y.; Pan, J.-W. Single quantum emitters in monolayer semiconductors. *Nat. Nanotechnol.* **2015**, *10*, 497–502.
- (8) Chakraborty, C.; Kinnischtzke, L.; Goodfellow, K. M.; Beams, R.; Vamivakas, A. N. Voltage-controlled quantum light from an atomically thin semiconductor. *Nat. Nanotechnol.* **2015**, *10*, 507–511.
- (9) Koperski, M.; Nogajewski, K.; Arora, A.; Cherkez, V.; Mallet, P.; Veuillen, J.-Y.; Marcus, J.; Kossacki, P.; Potemski, M. Single photon emitters in exfoliated WSe<sub>2</sub> structures. *Nat. Nanotechnol.* **2015**, *10*, 503–506.
- (10) Srivastava, A.; Sidler, M.; Allain, A. V.; Lembke, D. S.; Kis, A.; Imamoglu, A. Optically active quantum dots in monolayer WSe<sub>2</sub>. *Nat. Nanotechnol.* **2015**, *10*, 491–496.
- (11) Tonndorf, P.; Schmidt, R.; Schneider, R.; Kern, J.; Buscema, M.; Steele, G. A.; Castellanos-Gomez, A.; van der Zant, H. S. J.; Michaelis de Vasconcellos, S.; Bratschitsch, R. Single-photon emission from localized excitons in an atomically thin semiconductor. *Optica* 2015, 2, 347.

- (12) Kumar, S.; Kaczmarczyk, A.; Gerardot, B. D. Strain-Induced Spatial and Spectral Isolation of Quantum Emitters in Mono- and Bilayer WSe<sub>2</sub>. *Nano Lett.* **2015**, *15*, 7567–7573.
- (13) Shepard, G. D.; Ajayi, O. A.; Li, X.; Zhu, X.; Hone, J.; Strauf, S. Nanobubble induced formation of quantum emitters in monolayer semiconductors. 2D Mater. 2017, 4, 021019.
- (14) Palacios-Berraquero, C.; Kara, D. M.; Montblanch, A. R.-P.; Barbone, M.; Latawiec, P.; Yoon, D.; Ott, A. K.; Loncar, M.; Ferrari, A. C.; Atatüre, M. Large-scale quantum-emitter arrays in atomically thin semiconductors. *Nat. Commun.* **2017**, *8*, 15093.
- (15) Branny, A.; Kumar, S.; Proux, R.; Gerardot, B. D. Deterministic strain-induced arrays of quantum emitters in a two-dimensional semiconductor. *Nat. Commun.* **2017**, *8*, 15053.
- (16) Iff, O.; Tedeschi, D.; Martín-Sánchez, J.; Moczala-Dusanowska, M.; Tongay, S.; Yumigeta, K.; Taboada-Gutiérrez, J.; Savaresi, M.; Rastelli, A.; Alonso-González, P.; Höfling, S.; Trotta, R.; Schneider, C. Strain-Tunable Single Photon Sources in WSe<sub>2</sub> Monolayers. *Nano Lett.* **2019**, *19*, 6931–6936.
- (17) Luo, Y.; Shepard, G. D.; Ardelean, J. V.; Rhodes, D. A.; Kim, B.; Barmak, K.; Hone, J. C.; Strauf, S. Deterministic coupling of site-controlled quantum emitters in monolayer WSe<sub>2</sub> to plasmonic nanocavities. *Nat. Nanotechnol.* **2018**, *13*, 1137–1142.
- (18) Luo, Y.; Liu, N.; Li, X.; Hone, J. C.; Strauf, S. Single photon emission in WSe<sub>2</sub> up 160 K by quantum yield control. 2D Mater. **2019**, *6*, 035017.
- (19) Wang, G.; Chernikov, A.; Glazov, M. M.; Heinz, T. F.; Marie, X.; Amand, T.; Urbaszek, B. Colloquium: Excitons in atomically thin transition metal dichalcogenides. *Rev. Mod. Phys.* **2018**, *90*, 021001.
- (20) Zhou, Y.; Scuri, G.; Wild, D. S.; High, A. A.; Dibos, A.; Jauregui, L. A.; Shu, C.; Greve, K. D.; Pistunova, K.; Joe, A. Y.; Taniguchi, T.; Watanabe, K.; Kim, P.; Lukin, M. D.; Park, H. Probing dark excitons in atomically thin semiconductors via near-field coupling to surface plasmon polaritons. *Nat. Nanotechnol.* **2017**, *12*, 856–860.
- (21) Wang, G.; Robert, C.; Glazov, M. M.; Cadiz, F.; Courtade, E.; Amand, T.; Lagarde, D.; Taniguchi, T.; Watanabe, K.; Urbaszek, B.; Marie, X. In-Plane Propagation of Light in Transition Metal Dichalcogenide Monolayers: Optical Selection Rules. *Phys. Rev. Lett.* **2017**, *119*, 047401.
- (22) Edelberg, D.; et al. Approaching the Intrinsic Limit in Transition Metal Diselenides via Point Defect Control. *Nano Lett.* **2019**, *19*, 4371–4379.
- (23) Linhart, L.; Paur, M.; Smejkal, V.; Burgdörfer, J.; Mueller, T.; Libisch, F. Localized Intervalley Defect Excitons as Single-Photon Emitters in WSe<sub>2</sub>. *Phys. Rev. Lett.* **2019**, *123*, 146401.
- (24) Lieb, M. A.; Zavislan, J. M.; Novotny, L. Single-molecule orientations determined by direct emission pattern imaging. *J. Opt. Soc. Am. B* **2004**, *21*, 1210.
- (25) Lindlau, J.; Robert, C.; Funk, V.; Förste, J.; Förg, M.; Colombier, L.; Neumann, A.; Courtade, E.; Shree, S.; Taniguchi, T.; Watanabe, K.; Glazov, M. M.; Marie, X.; Urbaszek, B.; Högele, A. Identifying optical signatures of momentum-dark excitons in transition metal dichalcogenide monolayers. 2017, arXiv:1710.00988. arXiv.org e-Print archive. https://arxiv.org/abs/1710.00988.
- (26) He, M.; Rivera, P.; Tuan, D. V.; Wilson, N. P.; Yang, M.; Taniguchi, T.; Watanabe, K.; Yan, J.; Mandrus, D. G.; Yu, H.; Dery, H.; Yao, W.; Xu, X. Valley phonons and exciton complexes in a monolayer semiconductor. *Nat. Commun.* **2020**, *11*, 618.
- (27) Förste, J.; Tepliakov, N. V.; Kruchinin, S. Y.; Lindlau, J.; Funk, V.; Förg, M.; Watanabe, K.; Taniguchi, T.; Baimuratov, A. S.; Högele, A. Exciton g-factors in monolayer and bilayer WSe<sub>2</sub> from experiment and theory. 2020, arXiv:2002.11646. arXiv.org e-Print archive. https://arxiv.org/abs/2002.11646.
- (28) Robert, C.; Amand, T.; Cadiz, F.; Lagarde, D.; Courtade, E.; Manca, M.; Taniguchi, T.; Watanabe, K.; Urbaszek, B.; Marie, X. Fine structure and lifetime of dark excitons in transition metal dichalcogenide monolayers. *Phys. Rev. B: Condens. Matter Mater. Phys.* 2017, 96, 155423.

- (29) Srivastava, A.; Sidler, M.; Allain, A. V.; Lembke, D. S.; Kis, A.; Imamoglu, A. Valley Zeeman effect in elementary optical excitations of monolayer WSe<sub>2</sub>. *Nat. Phys.* **2015**, *11*, 141–147.
- (30) Koperski, M.; Molas, M. R.; Arora, A.; Nogajewski, K.; Bartos, M.; Wyzula, J.; Vaclavkova, D.; Kossacki, P.; Potemski, M. Orbital, spin and valley contributions to Zeeman splitting of excitonic resonances in MoSe<sub>2</sub>, WSe<sub>2</sub> and WS<sub>2</sub> Monolayers. 2D Mater. 2019, 6, 015001.
- (31) Darlington, T. P.; Carmesin, C.; Florian, M.; Yanev, E.; Ajayi, O.; Ardelean, J.; Rhodes, D. A.; Ghiotto, A.; Krayev, A.; Watanabe, K.; Taniguchi, T.; Kysar, J. W.; Pasupathy, A. N.; Hone, J. C.; Jahnke, F.; Borys, N. J.; Schuck, P. J. Imaging strain-localized exciton states in nanoscale bubbles in monolayer WSe<sub>2</sub> at room temperature. 2020, arXiv:2003.01789. arXiv.org e-Print archive. https://arxiv.org/abs/2003.01789.
- (32) Rogobete, L.; Kaminski, F.; Agio, M.; Sandoghdar, V. Design of plasmonic nanoantennae for enhancing spontaneous emission. *Opt. Lett.* **2007**, 32, 1623.
- (33) Akselrod, G. M.; Argyropoulos, C.; Hoang, T. B.; Cirací, C.; Fang, C.; Huang, J.; Smith, D. R.; Mikkelsen, M. H. Probing the mechanisms of large Purcell enhancement in plasmonic nanoantennas. *Nat. Photonics* **2014**, *8*, 835–840.
- (34) Russell, K. J.; Liu, T.-L.; Cui, S.; Hu, E. L. Large spontaneous emission enhancement in plasmonic nanocavities. *Nat. Photonics* **2012**, *6*, 459–462.
- (35) Luo, Y.; Ahmadi, E. D.; Shayan, K.; Ma, Y.; Mistry, K. S.; Zhang, C.; Hone, J.; Blackburn, J. L.; Strauf, S. Purcell-enhanced quantum yield from carbon nanotube excitons coupled to plasmonic nanocavities. *Nat. Commun.* **2017**, *8*, 1413.
- (36) Kinkhabwala, A.; Yu, Z.; Fan, S.; Avlasevich, Y.; Müllen, K.; Moerner, W. E. Large single-molecule fluorescence enhancements produced by a bowtie nanoantenna. *Nat. Photonics* **2009**, *3*, 654–657.
- (37) Shayan, K.; Liu, N.; Cupo, A.; Ma, Y.; Luo, Y.; Meunier, V.; Strauf, S. Magnetic Proximity Coupling of Quantum Emitters in WSe<sub>2</sub> to van der Waals Ferromagnets. *Nano Lett.* **2019**, *19*, 7301–7308.
- (38) Mermillod, Q.; Jakuiczyk, T.; Delmonte, V.; Delga, A.; Peinke, E.; Gérard, J.-M.; Claudon, J.; Kasprzak, J. Harvesting, Coupling, and Control of Single-Exciton Coherences in Photonic Waveguide Antennas. *Phys. Rev. Lett.* **2016**, *116*, 163903.
- (39) Luo, Y.; He, X.; Kim, Y.; Blackburn, J. L.; Doorn, S. K.; Htoon, H.; Strauf, S. Carbon Nanotube Color Centers in Plasmonic Nanocavities: A Path to Photon Indistinguishability at Telecom Bands. *Nano Lett.* **2019**, *19*, 9037.